INL/EXT-20-59600
Revision 0

Light Water Reactor Sustainability Program

Hybrid Modeling of a Circulating Water Pump Motor

August 2020

U.S. Department of Energy

Office of Nuclear Energy

INL/EXT-20-59600
Revision 0

Hybrid Modeling of a Circulating Water Pump Motor

Vivek Agarwal
Idaho National Laboratory

Sasa Kovacevic
Washington State University

Palas Harry
Public Service Enterprise Group (PSEG) Nuclear, LLC

August 2020

Prepared for the
U.S. Department of Energy
Office of Nuclear Energy
Under DOE Idaho Operations Office
Contract DE-AC07-05ID14517

ABSTRACT

To achieve high-capacity factors, the nuclear fleet has relied on labor-intensive and time-consuming operation and preventive maintenance programs for plant systems. Manually-performed inspection, calibration, testing, and maintenance of plant assets at periodic frequencies, along with the time-based replacement of assets irrespective of condition, have resulted in a costly, *labor-centric business model.*

Fortunately, there are technologies that can eliminate unnecessary preventive maintenance activities by deploying risk-informed predictive maintenance, enabling the transition to a *technology-centric business model*. The technology-centric business model will enable plants to optimize and automate maintenance activities, leading to cost reductions, since labor is a rising cost and technology is a declining cost. The implementation of scalable technologies and methodologies across plant systems and across the nuclear fleet is critical for the successful deployment of a risk-informed predictive maintenance strategy at commercial nuclear power plants.

The work presented in this report is being developed as part of a collaborative research effort between Idaho National Laboratory and Public Service Enterprise Group Nuclear, LLC. It describes the technical basis to develop a digital twin of the circulating water pump motor, using a hybrid modeling approach in order to capture both the deterministic and stochastic operation characteristics. A detailed first principle model of the circulating water pump motor is developed using the multipurpose finite element software COMSOL Multiphysics. Geometry and material properties were obtained from the circulating water system manual. The actual vibration measurements used to compare with the simulated vibration response and to train the data-driven approach were obtained from installed wireless vibration sensors. The outcomes of the report lay the foundation to develop a comprehensive digital twin of the circulating water system by taking into consideration different operating dynamics. The path forward for this research includes (1) enhancing the hybrid model by relaxing some of the assumptions and its evaluation and (2) utilizing the hybrid model to develop predictive fault signatures, enabling development of robust diagnosis and prognosis models for circulating water system health and decision-making capabilities as part of the predictive maintenance strategy.

ACKNOWLEDGEMENTS

This report was made possible through funding by the United States Department of Energy's Light Water Reactor Sustainability Program. We are grateful to Alison Hahn of the United States Department of Energy and Bruce P. Hallbert and Craig A. Primer at Idaho National Laboratory for championing this effort. We appreciate the technical guidance of Daniel Cossu at Public Service Enterprise Group (PSEG) Nuclear, LLC on developing numerical circulating water pump motor model. We thank Katie Stokes at Idaho National Laboratory for the technical editing and formatting of this report.

CONTENTS

FIGURES

TABLES

ACRONYMS

CM	corrective maintenance
CWP	circulating water pump
CWS	circulating water system
INL	Idaho National Laboratory
LWR	light water reactor
LWRS	Light Water Reactor Sustainability
MIB	motor inboard bearing
MOB	motor outboard bearing
NPP	nuclear power plant
O&M	operation and maintenance
PdM	predictive maintenance
PM	preventive maintenance
PSD	power spectral density
PSEG	Public Service Enterprise Group
R&D	research and development
RMSE	root mean square error
TERMS	Technology-Enable Risk-Informed Maintenance Strategy
VSN	vibration sensor node

HYBRID MODELING OF A CIRCULATING WATER PUMP MOTOR

1. INTRODUCTION AND MOTIVATION

The primary objective of the research presented in this report is to develop a hybrid model of a circulating water pump (CWP) motor to support risk-informed predictive maintenance (PdM) strategy taking advantage of advancements in data analytics, machine learning, artificial intelligence, and visualization. As well-constructed PdM approaches rely on machine learning based predictive capability which are purely data driven. In this report, hybrid modeling approach is aimed at capturing the first principle information of the CWP motor operation along the information extracted from the measured data. This would enhance the reliability of the PdM strategy by reducing the dependency on data. This would allow commercial nuclear power plants (NPPs) to achieve a reliable transition from current labor-intensive preventive maintenance (PM) programs to a technology-driven PdM program, as shown in Figure 1, eliminating unnecessary operation and maintenance (O&M) costs. Over the years, the nuclear fleet has relied on labor-intensive and time-consuming PM programs, driving up O&M costs to achieve a high-capacity factor.

Figure 1. Transition from a PM program to a risk-informed PdM program.

The hybrid modeling approach for a circulating water system (CWS) presented in this report was developed by Idaho National Laboratory (INL) in collaboration with Public Service Enterprise Group (PSEG) Nuclear, LLC. The CWS is an important non-safety-related system and is omnipresent across the fleet of existing light-water nuclear plants. Traditionally, most of the PdM approaches in the nuclear industry are developed at the component level [1–5] by taking into account plant process data, manual measurements, and historical failure records. This approach depends on available data and the frequency at which it is measured. This approach does not incorporate the physics-based information related to plant asset structure and operation. The research approach presented in this report addresses these limitations. The hybrid modeling approach presented in this report combines both the deterministic (via first principle modeling) and the stochastic (via data-driven modeling) operation characteristics of the CWP motor.

The research and development (R&D) and outcomes reported here are part of the Technology-Enabled Risk-Informed Maintenance Strategy (TERMS) Project sponsored by the U.S. Department of

Energy's Light Water Reactor Sustainability (LWRS) program. The LWRS program is an R&D program conducted in close partnership with industry to provide the technical foundations for licensing, managing, and economically operating the current fleet of NPPs. The LWRS program serves to help the U.S. nuclear industry adopt new technologies and engineering solutions.

Within the LWRS program, the Plant Modernization Pathway conducts targeted R&D to address aging and reliability concerns with legacy instrumentation and control systems through modernized technologies for the existing U.S. fleet of operating light-water reactors (LWRs) and improved processes for plant operation and power generation. The research goals of the Plant Modernization Pathway are focused on delivering technologies and results that significantly reduce the technical, financial, and regulatory risk of modernization.

To achieve both LWRS program and Plant Modernization Pathway goals [5], a series of pilot projects is underway to develop and demonstrate new technologies that can affect transformative change in the operations and support of nuclear plants. The TERMS pilot project is developing the necessary technologies and methodologies to achieve performance improvement through a transformative transition to PdM.

This report is organized as follows:

- Section 2 introduces the hybrid modeling approach.
- Section 3 summarizes the collection of vibration data using the wireless vibration sensors installed on CWP motors.
- Section 4 describes the first principle modeling of CWS.
- Section 5 presents the discussion on simulated vibration response obtained from the first principle model of CWP motor and its comparison with actual measured vibration signals.
- Section 6 describes how the difference between the simulated and measured vibration responses along with inputs to the first principle model can be utilized to develop a data-driven approach.
- Section 8 summaries the research accomplishments and presents a path forward in advancing R&D activities.

2. HYBRID MODELING

Hybrid or semiparametric models consist of model structures that combine first principles and data-driven sub-models based on different knowledge sources. The development of a hybrid semiparametric model can offer a number of advantages over traditional first-principles or data-driven modeling. These advantages, such as broader knowledge base, transparency of the modeling approach, and cost-effective model development, have been widely recognized in many industries such as chemical and biomedical engineering [7, 8].

First-principles modeling and data-driven modeling constitute two approaches which usually rely on different sources of information and different principles [9]. While the development of a first-principle model is very time consuming and requires detailed knowledge of the domain, data-driven methods can be quickly applied to the problem at hand and require very little knowledge about the process. However, in comparison to first-principles models, data-driven models require availability of a large amount of recent data, and they are usually only applicable in the vicinity to those regions for which they were developed. Hybrid semiparametric modeling capitalizes on the advantages and disadvantages of strictly first principles and data-driven modeling. A schematic of a hybrid modeling approach is shown in Figure 2.

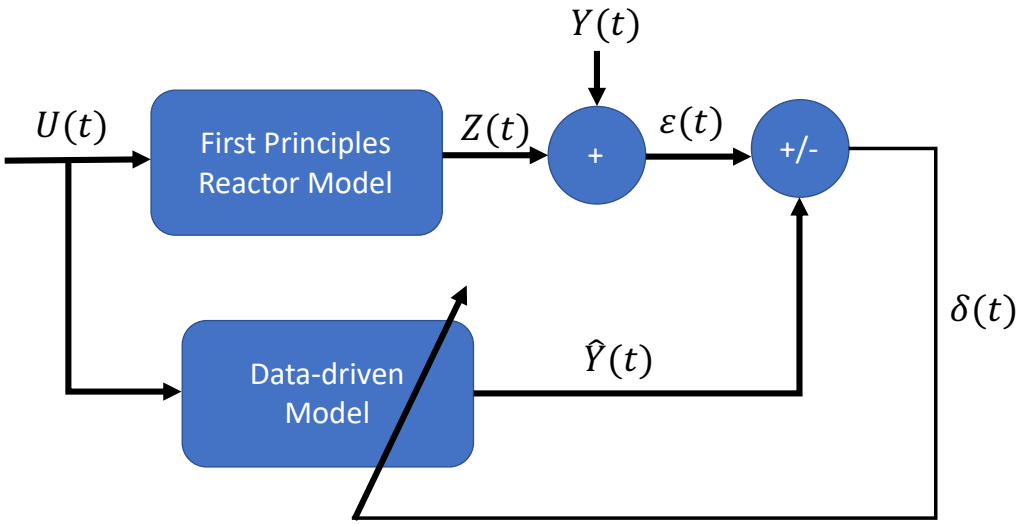

Figure 2. A schematic representation of hybrid approach to system modeling.

Based on the hybrid modeling approach, a first-principle model of the CWP motor will be developed. Inputs to the model, denoted as $U(t)$, will be manipulated to generate the simulated vibration waveforms, denoted as $Z(t)$. The simulated waveforms, $Z(t)$, will be compared with actual vibration waveforms, denoted as $Y(t)$, measured using installed wireless vibrations sensors on PSEG-owned Salem's CWP motors. The error between the measured and simulated waveforms, denoted as $\varepsilon(t)$, and $U(t)$ will be used to train the data-driven model. The predicted outcome of the data-driven model, denoted as $\hat{Y}(t)$, is the prediction of the $\varepsilon(t)$. In Figure 2, $\delta(t)$ is the residual between $\hat{Y}(t)$ and $\varepsilon(t)$.

3. WIRELESS VIBRATION SENSOR

Vibration monitoring instrumentation contains accelerometers that sense changes in the amplitude and frequency of dynamic forces that can impair rotating equipment. Identifying degradation at its onset by analyzing vibration measurements allows personnel to identify issues, such as imbalance, looseness, misalignment, or bearing wear in assets prior to significant degradation and failure. This gives the plant more options and more time to respond, allowing for more effective resolutions.

Periodic vibration measurements are collected on a CWP motor. The collection of continuous vibration measurements as part of the CWS process data enhances the diagnosis and prognosis of CWP motor conditions. This aligns with the objective of achieving PdM on plant assets in commercial NPPs. To achieve the objective, the team decided to continuously monitor the CWP motors using wireless vibration sensor nodes from KCF Technologies. The installed models are Vibration Sensor Node (VSN) (i.e., SD-VSN-3) [10]. Sixty VSN-3 sensor nodes have been installed across 12 CWP motors and associated CWP bypass valves at Salem NPP. Three wireless VSNs are installed on each CWP motor and two sensors on the associated CWP bypass valve at the plant site. Two VSNs are also installed on the associated pump valve. Each sensor node consists of two accelerometers sensitive to orthogonal in-plane motion and a temperature sensor. The sensor nodes can be mounted on to the plant asset either via a magnetic base in the node or a mounting plate attached using epoxy. PSEG uses magnetic mounting of the sensor nodes.

The KCF Technologies wireless sensing system and its components are shown in Figure 3 [10, 11]. A cloud configuration was installed at the Salem plant site to support the deployment of wireless sensor nodes on CW pumps and motors. The sensor node transmits X- and Y-direction vibration data along with temperature data to the base station over a cellular network which then transmits the data using the PSEG

Wi-Fi network to the KCF cloud. The data stored in the cloud is accessed through KCF SMARTDiagnostics® (SD) machine condition monitoring software. SMARTDiagnostics® provides an interface to visualize the data and the state of the equipment as well as the ability to export the data to a text file.

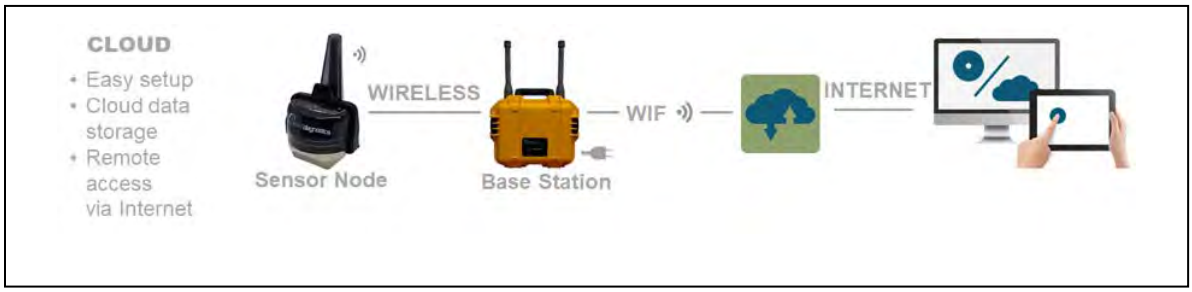

Figure 3. The KCF wireless sensing system and its components [8, 9].

3.1 Wireless Vibration Sensor Node Installation on Circulating Water System

The KCF SD-VSN-3 sensors were installed on August 23, 2019. Each CWP motor system has five SD-VSN-3s mounted on the assets. Three VSNs have been installed on each CWP motor adjacent to vibration measurement locations labeled as inboard node, outboard node, and top node in Figure 4.

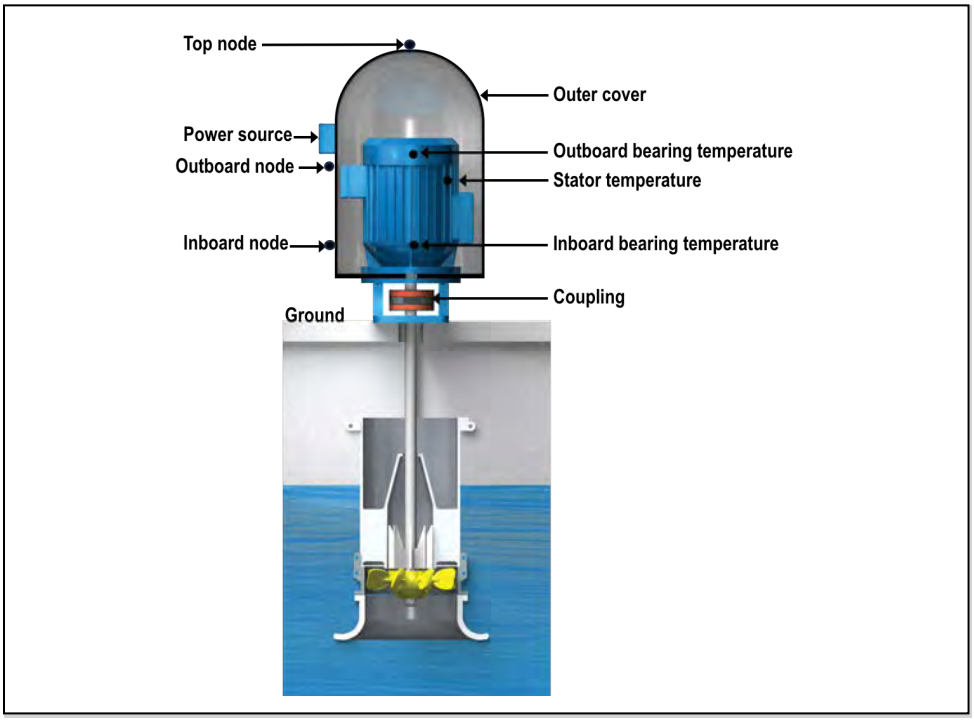

Figure 4. Mounting locations of the VSN nodes on the CWP motor.

Figure 5 shows the relative location of the VSNs on the side of the motor outer covering for the 12 CWP motors. The VSNs are placed as close as possible to the buttons that have been used for the PSEG historical data monitoring inboard and outboard vibrations. The historical vibration measurements are taken on these locations every 3 months. The VSN-recorded vibration data will be compared with the historical vibration data to ensure they are capturing data and performing as expected. The top VSN captures both in-plane vibrations at the same time. The representative location of the top VSN for all

CWP motors is shown in Figure 6. For details on installation of KCF VSNs and data acquisition specifications, refer to [12].

In this research project, real-time vibration data from motor inboard and motor outboard locations alone will be compared with the simulated vibration signal that is generated using the first principle model of the CWP motor (see Section 4).

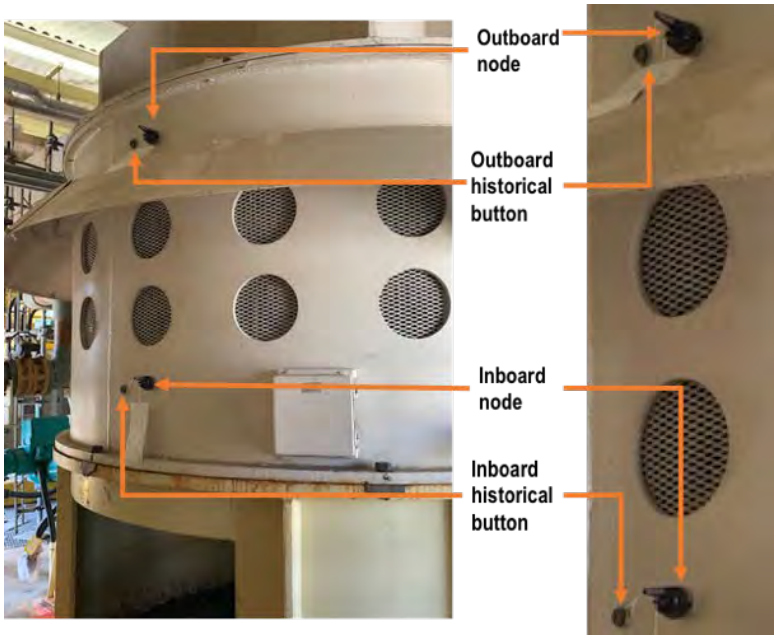

Figure 5. Motor inboard and motor outboard measuring locations with KCF sensors.

Figure 6. A VSN mounted on top of the CW motor cover in line with the historical buttons.

3.2 Vibration Data

The installed KCF VSNs transmit data every 15 minutes to the KCF cloud. These are known settings. The sampling frequency of each sensor is set to 512 Hz and the measurement duration of the acquired vibration time waveform is 3200 milliseconds. The data is collected at motor inboard bearing (MIB) and motor outboard bearing (MOB) locations under normal working conditions. For the sake of brevity, only five vibration waveforms at each location in each direction are presented and discussed in this report. The collected waveforms in *g* are normalized (i.e., mean value is 0 and the standard deviation is 1) and are

shown in Figure 7–Figure 10. The acceleration plots in Figure 7 show that the maximum acceleration magnitude for vertical acceleration is around ±1.5g at the MIB location. A similar observation can be noticed for vertical acceleration at the MOB location (Figure 9). However, Figure 8 and Figure 10 show that the vibration magnitude for radial acceleration is above ±2.0g and the results are more scattered compared to the vertical vibration plots.

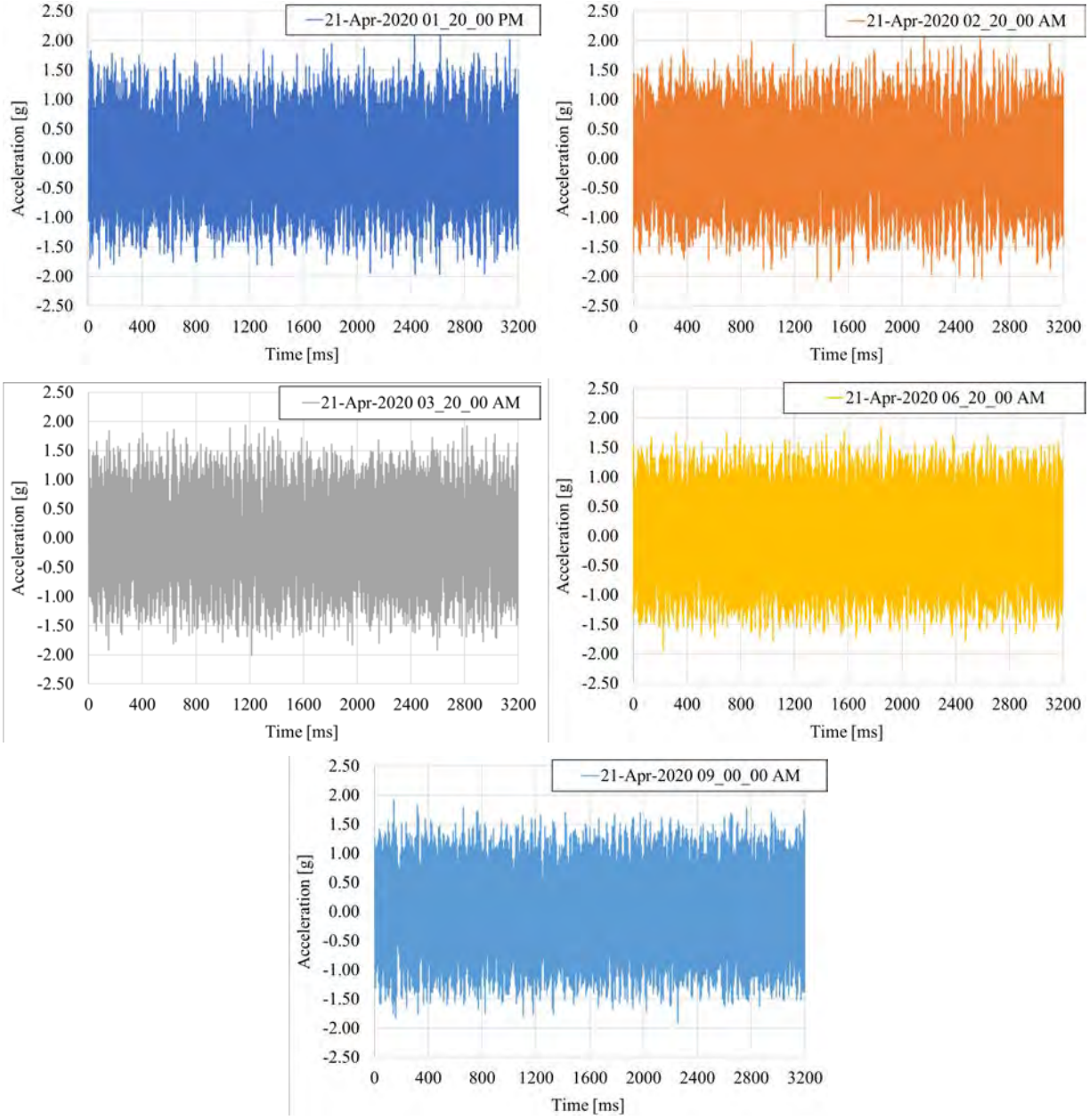

Figure 7. Vertical (axial) acceleration for the MIB location collected at different time instances.

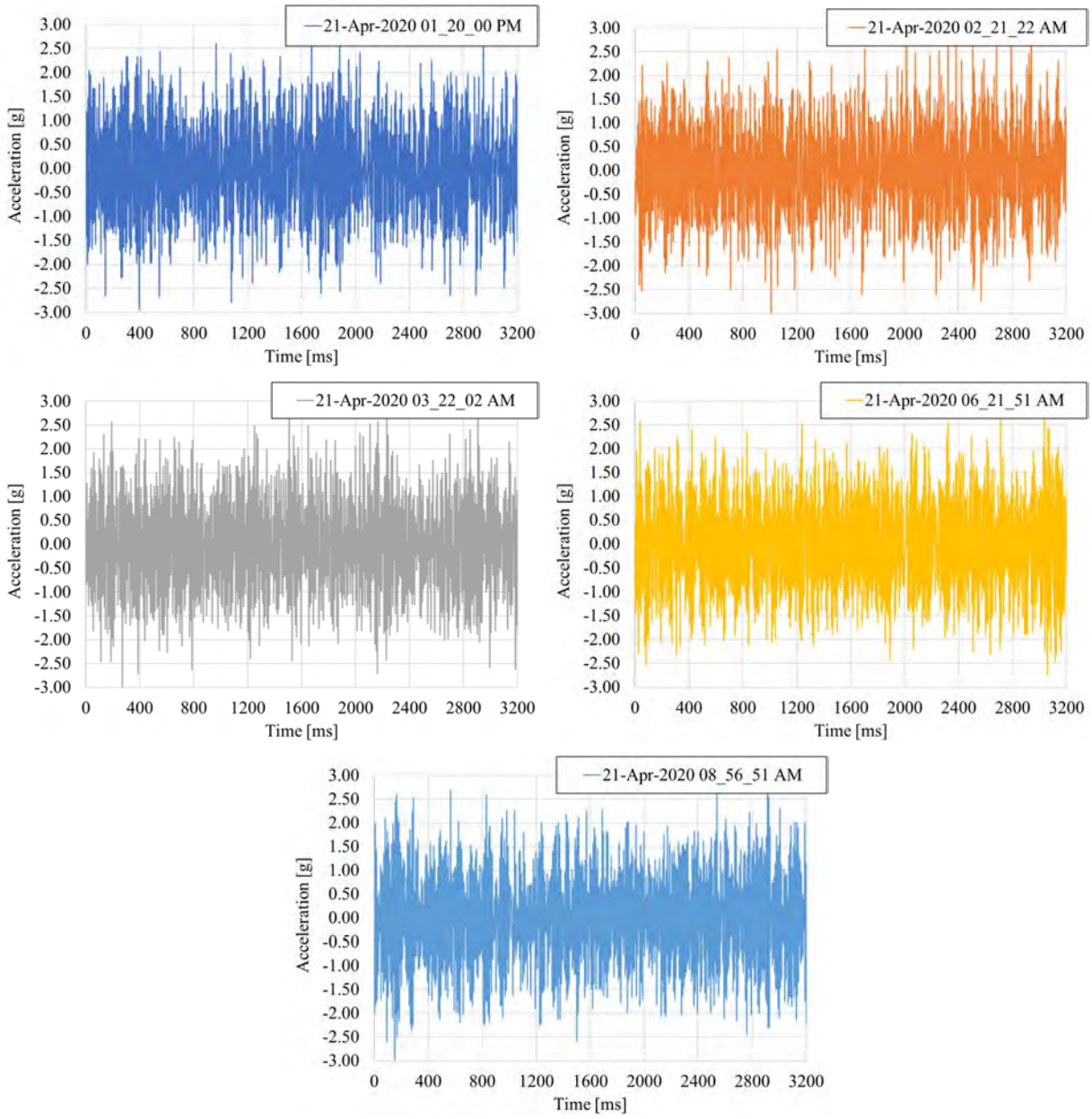

Figure 8. Radial acceleration for the MIB location collected at different time instances.

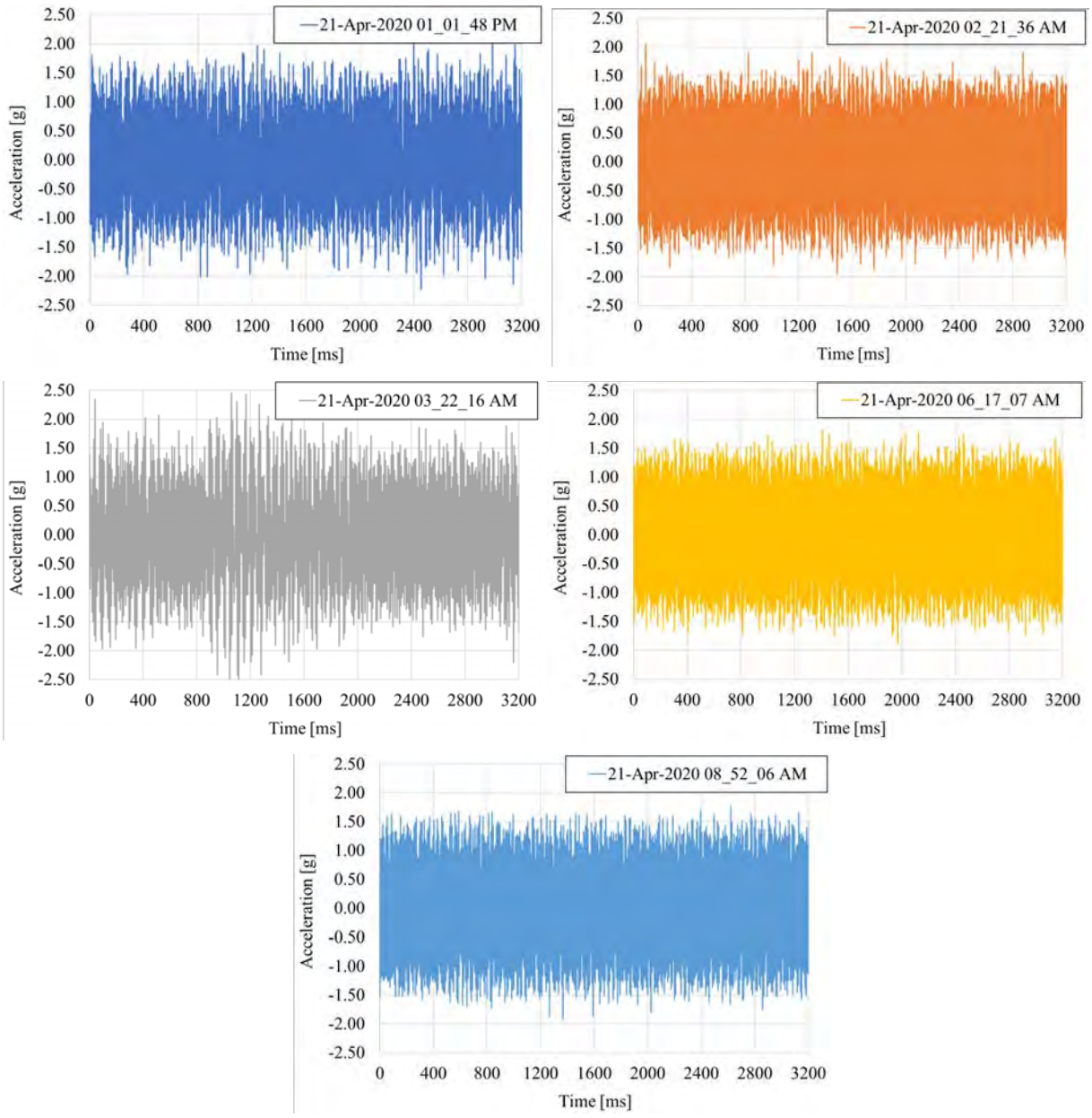

Figure 9. Vertical (axial) acceleration for the MOB location collected at different time instances.

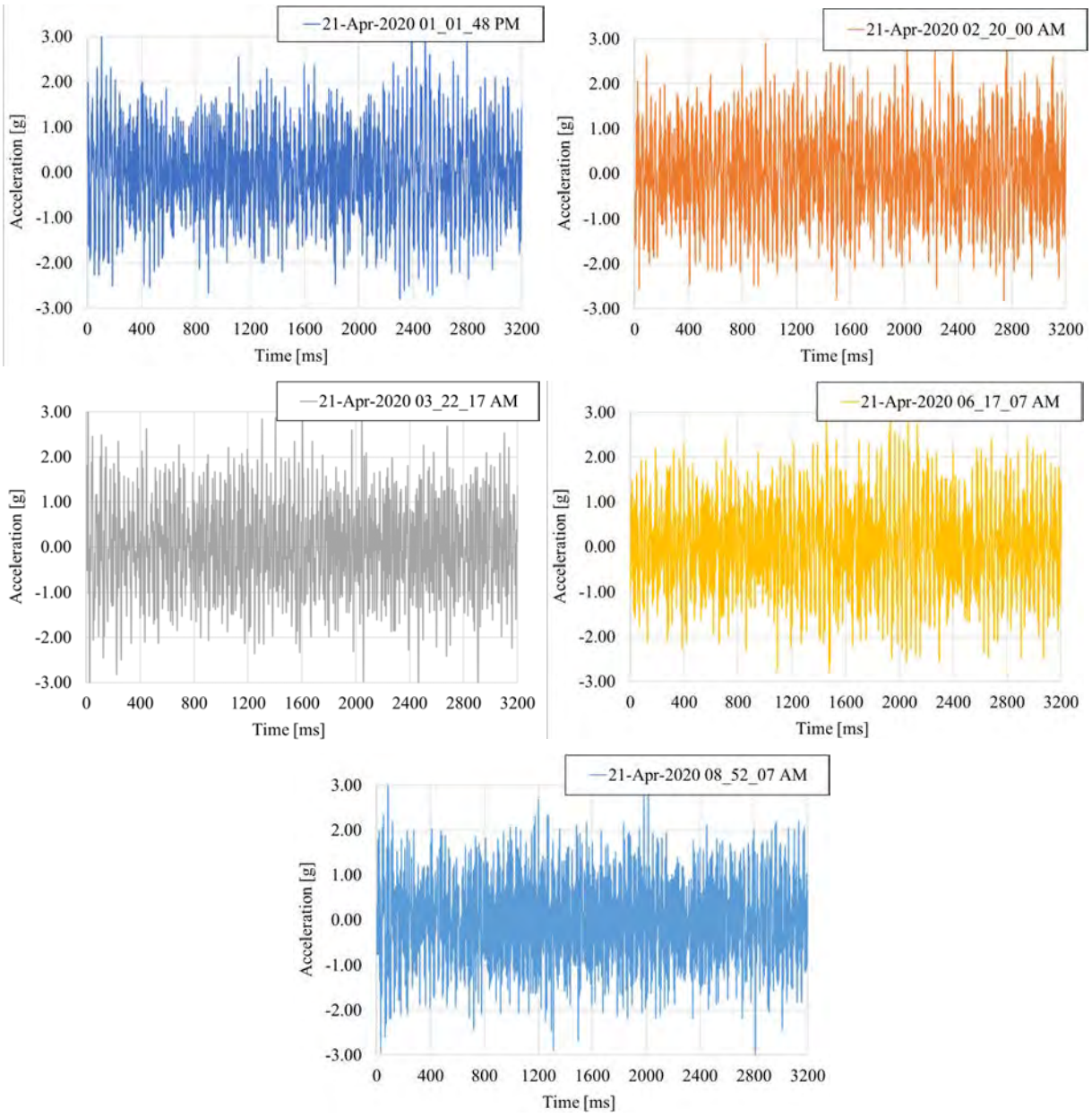

Figure 10. Radial acceleration for the MOB location collected at different time instances.

Frequency analysis of the vibration waveform is performed and a power spectral density (PSD) is generated. The PSD plots are a useful signal-processing approach because they display magnitude variations over a range of frequencies. The PSD plots are presented in Figure 11–Figure 14 corresponding to the time waveforms shown in Figure 7–Figure 10.

As one can observe from Figure 11 and Figure 13, which show vertical acceleration at the MIB and MOB locations, three dominant frequencies are present (i.e., 30 Hz, 100 Hz, and the most dominant frequency of 120 Hz). Figure 12 and Figure 14 show radial acceleration. Notice these figures show many different frequencies with different intensities, especially for the MOB-measuring location (Figure 9). However, it is also interesting to see in Figure 12 and Figure 14 two dominant frequencies at 30 and 120 Hz, which are also the most dominant frequencies at the MIB- and MOB-measuring locations for vertical accelerations (Figure 11 and Figure 13).

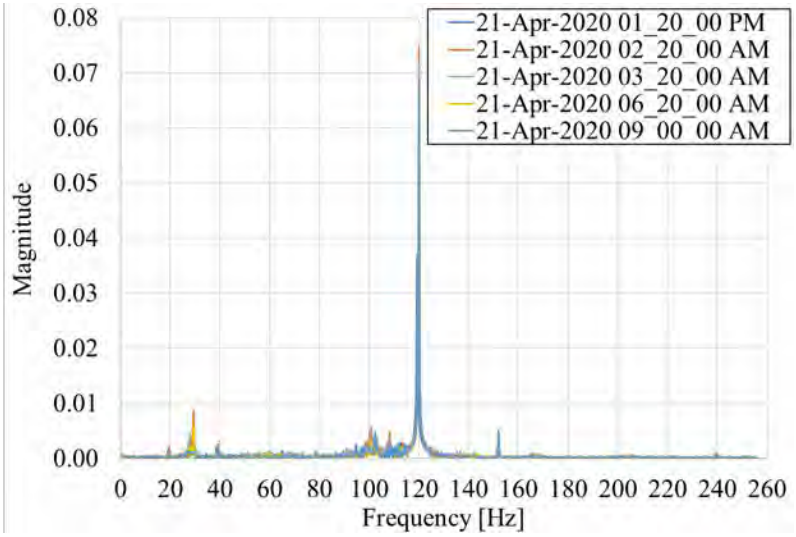

Figure 11. PSD plot for vertical (axial) acceleration for the MIB.

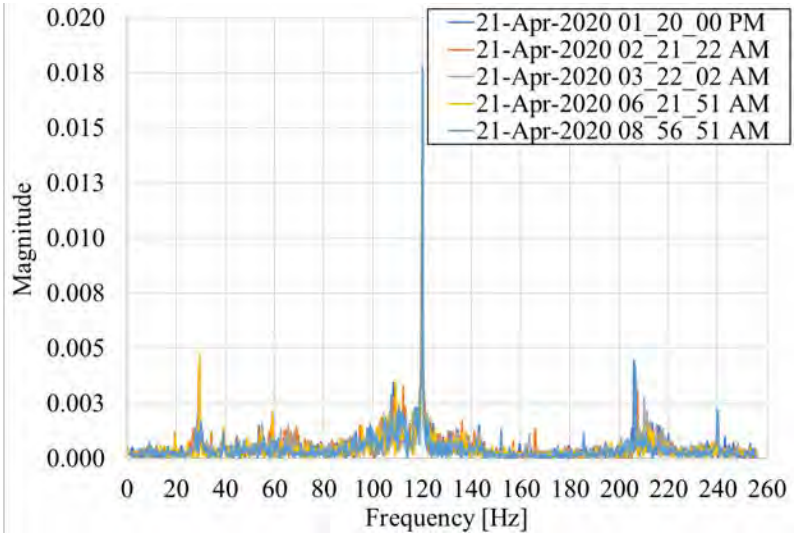

Figure 12. PSD plot for radial acceleration for the MIB location.

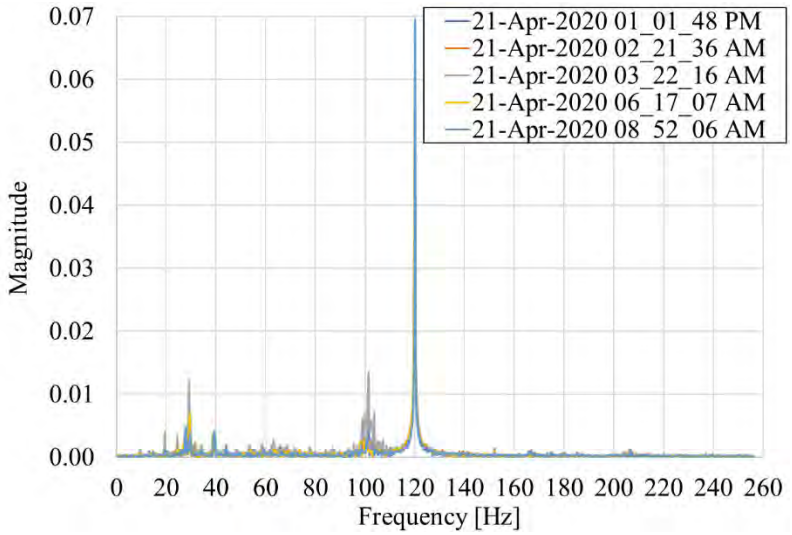

Figure 13. PSD plot for vertical (axial) acceleration for the MOB location.

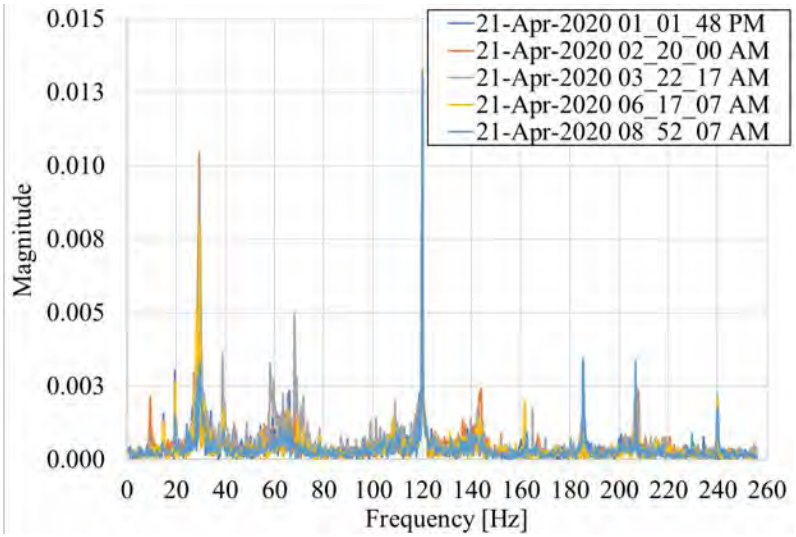

Figure 14. PSD plot for radial acceleration for the MOB location.

4. THE FINITE ELEMENT MODEL

The structural vibration response of the whole system is simulated using the multipurpose finite element software COMSOL Multiphysics. A nonlinear transient dynamic analysis is employed in order to find the structural behavior of the system. All geometry parts (motor casing, casing cover, and motor stand) are generated and assembled in the COMSOL Multiphysics. The following sections give more details on modeling and results. The numerically obtained vibration waveforms in *g* for both MIB and MOB locations and for both directions (axial and radial) are given in Section 4.4, followed by the PSD plots.

4.1 Geometry and Material Properties

The geometry of the motor casing, casing cover, and motor stand is determined using the manufacturer's manual of the CWP motor and is incorporated into the numerical model. Some other geometry details not available in the manufacturer's manual (thickness of the casing, vertical stiffeners for the motor stand, size of the motor ventilation holes on motor casing, stiffeners, and thickness of the

casing cover, etc.) were estimated based on discussion and pictures provided by the PSEG CWP motor expert. All main geometry dimensions are tabulated in Table 1. The entire numerical model (consisting of the motor casing, casing cover, and motor stand) is given in Figure 15.

Table 1. Geometry dimensions for the considered CWP.

Geometry	**Size [in]**	**Geometry**	**Size [in]**
Casing outer diameter	104	Lower bearing outer diameter	22
Casing height	46.5	Lower bearing housing height	7
Casing thickness	1	Shaft diameter	7.875
Ventilation hole diameter	8	Rotor height	23
Hole diameter in lower bearing plate	10	Rotor diameter	71
Lower bearing plate thickness	1.25	Stator inner diameter	71.25
Motor stand height	40	Stator outer diameter	85
Casing cover height	33	Casing cover thickness	0.5

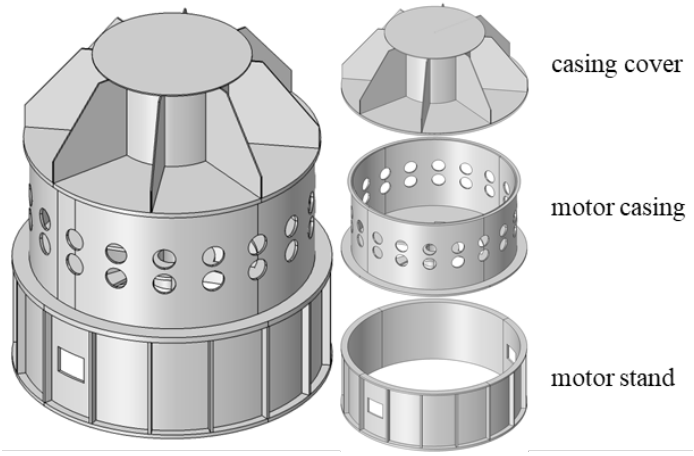

Figure 15. The whole computational domain consisting of the motor casing, casing cover, and motor stand.

For modeling purposes, all parts of the numerical model (motor casing, casing cover, and motor stand) are modeled using a homogenous material with the properties of standard constructional steel (i.e., Young's modulus E=210 GPa, Poisson ratio ν=0.3, and density ρ=7850 kg/m^3, as listed in Table 2).

Table 2. Material properties used in the simulation for the motor casing, casing cover, and motor stand.

Material	Elastic Modulus [GPa]	Poisson ratio	Density[kg/m^3]
Steel	210	0.3	7850

4.2 Boundary conditions and loads

The boundary conditions were assigned so they correspond to the actual supporting conditions (i.e., the motor stand is bolted into a concrete slab). Since the supporting bolts are equally spaced, the entire supporting surface (between the motor stand and concrete slab) was fully constrained (all three displacement components were set to 0) and the actual bolts were not included in the numerical model, as shown in Figure 16. No other boundary constraints were included in the finite element model.

The motor stand and motor casing are also connected with bolts placed at equal distance; therefore, both parts are modeled as a single part and no contact behavior is included. The same argument is valid

for the motor casing and casing cover connection. All three parts were modeled as a single domain with the above-mentioned boundary condition between the motor stand and concrete slab.

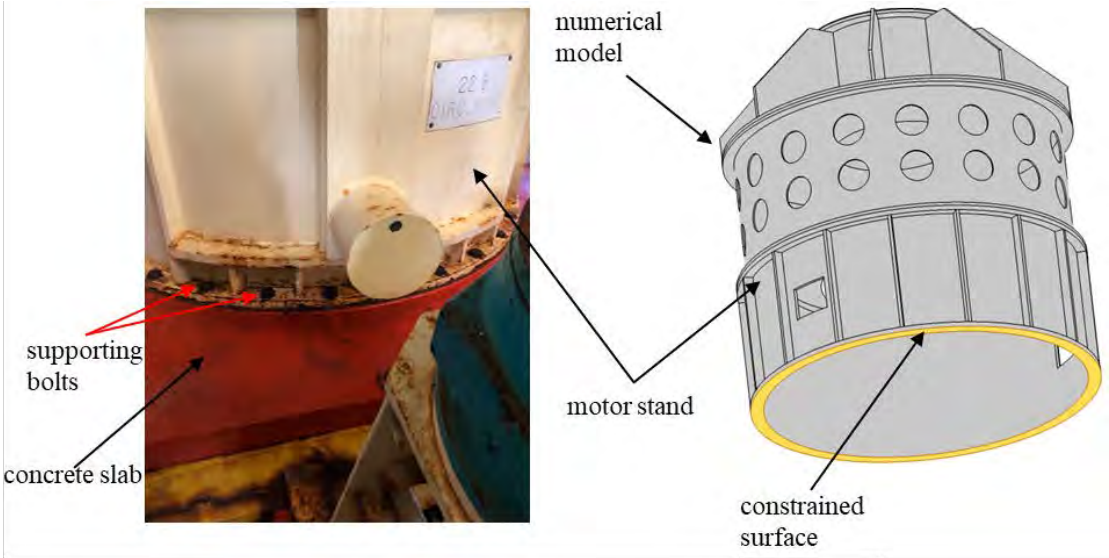

Figure 16. Boundary conditions applied on the motor stand. The bottom surface (marked in yellow) was fully constrained (all displacement components are equal to zero).

Some of the common vibratory forces observed in vertical pump motors include mass unbalance, misalignment of the coupling, mechanical action of the pump shaft and impeller, or even hydraulic action of fluid. Unfortunately, these force sources are unavoidable in real applications and they can cause high-vibration conditions. Modeling such a complicated system is challenging, which usually results in computationally intensive simulations both with respect to time and resources. Thus, to simplify the modeling task, some assumptions were introduced.

It is assumed that all submersible parts of the CWS do not contribute to motor vibration. As a result, all potential hydraulic-induced vibration of fluid and fluid-structure interaction, including mechanical interaction between pump shaft and impeller (below the mounting surface), are not considered. Only parts above the mounting surface, as shown in Figure 15 and Figure 16, are considered.

The motor shaft (which passes through the rotor and stator) is mounted in the top and lower bearing housings (shown in Figure 17 and Figure 18). A certain degree of misalignment between the motor shaft and these bearing housings are assumed, which allows some variance of the rotating axis in relation to the principal axis of inertia. This slightly eccentric configuration will unbalance mass, which in turn generates mechanical forces to the system. The vibration waveforms presented in Section 3 are actual measurements including all hydraulic and mechanical interactions contributing to the vibration. Thus, the forces used in the numerical model may be different than actual forces (due to many assumptions) in order to achieve the same acceleration magnitudes. We estimated these forces to be around 62 kilopounds (kip).

Therefore, the estimated loads generated during normal working motor conditions (i.e., at a running speed of 4.9 Hz) are introduced into the system at two locations (i.e., at the lower and upper bearing which are located in the lower and upper casing bearing plate, see Figure 18).

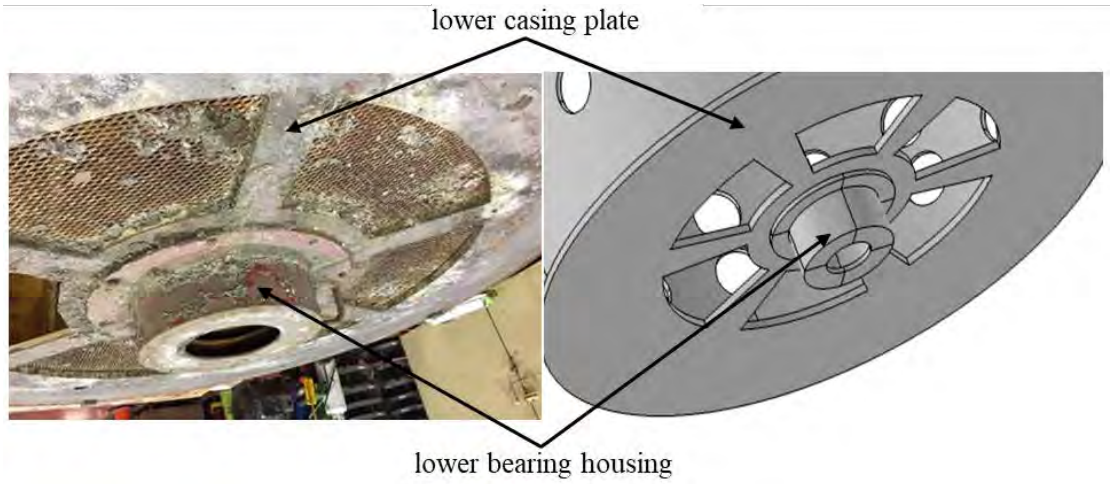

Figure 17. Lower casing bearing plate with bearing housing.

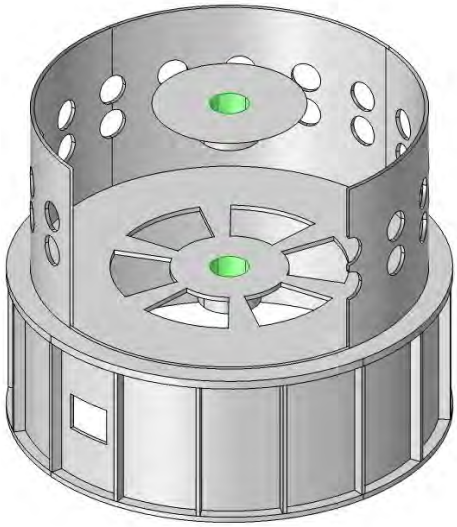

Figure 18. Top and bottom bearings where mechanical loads are introduced in the numerical model. Some geometry attributes are hidden for presentation purposes.

4.3 Finite element mesh

The entire computational domain (motor casing, casing cover, and motor stand) are meshed using an extremely fine element mesh with linear tetrahedron elements. The finite element mesh is shown in Figure 19. The entire numerical model contained approximately 600,000 DOFs.

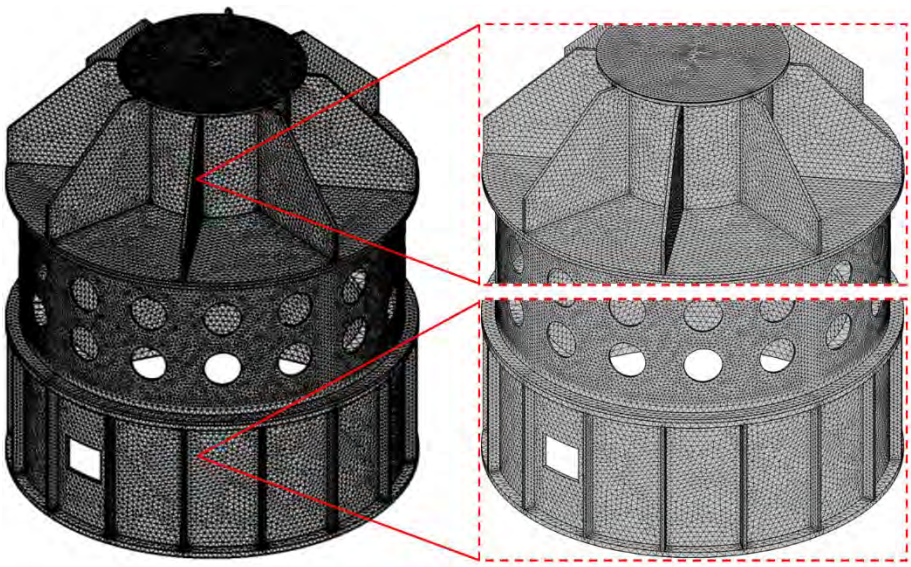

Figure 19. The entire computational domain with adapted finite element mesh.

4.4 Numerical results

The obtained vibrational responses using the presented numerical model are compared with the vibration measurements presented in Section 3. The numerically obtained vibration responses for both MIB- and MOB-measuring locations and for both axial and radial directions are normalized (such that the mean value is 0 and the standard deviation is 1). In order to present this comparison between numerically and experimentally obtained vibrational responses more clearly, only a time-span of 1000 milliseconds (from 1000 to 2000 ms) will be used. This visual comparison is given in Figure 20–Figure 23 for both MIB- and MOB-measuring locations.

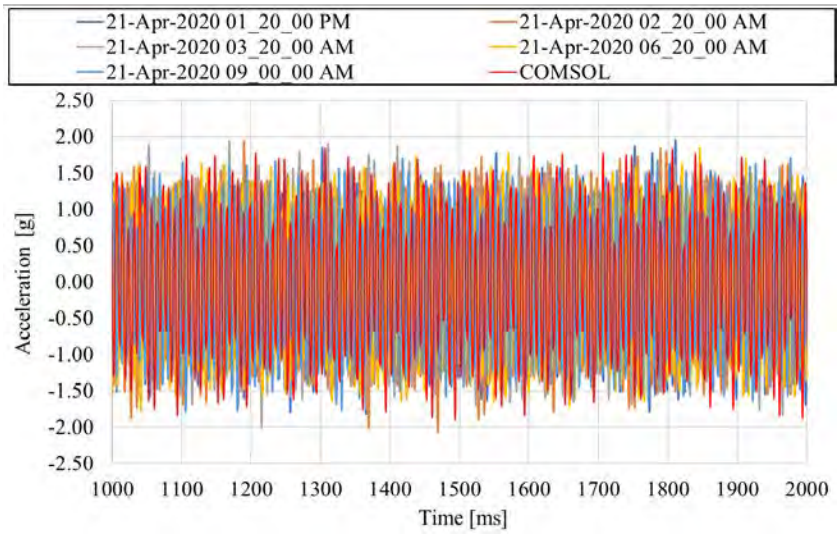

Figure 20. Vertical (axial) acceleration for the MIB location collected at five different time instances and the simulated vibration waveform.

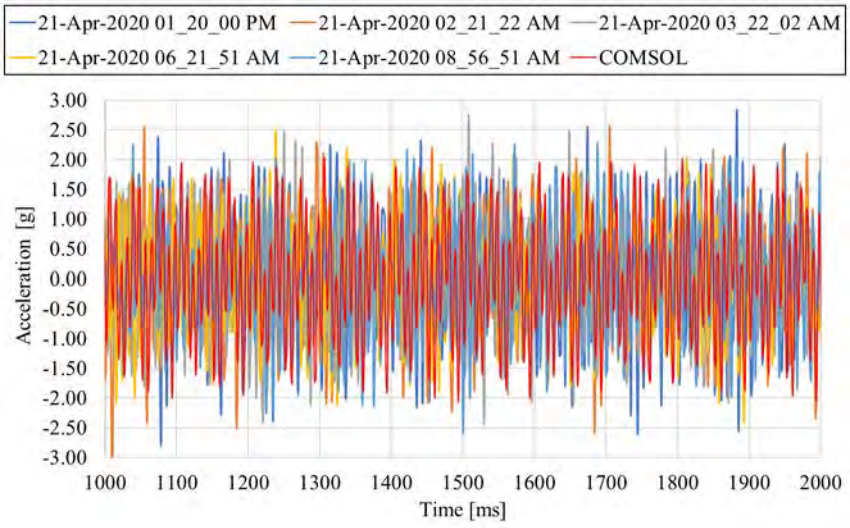

Figure 21. Radial acceleration for the MIB location collected at five different time instances and the simulated vibration waveform.

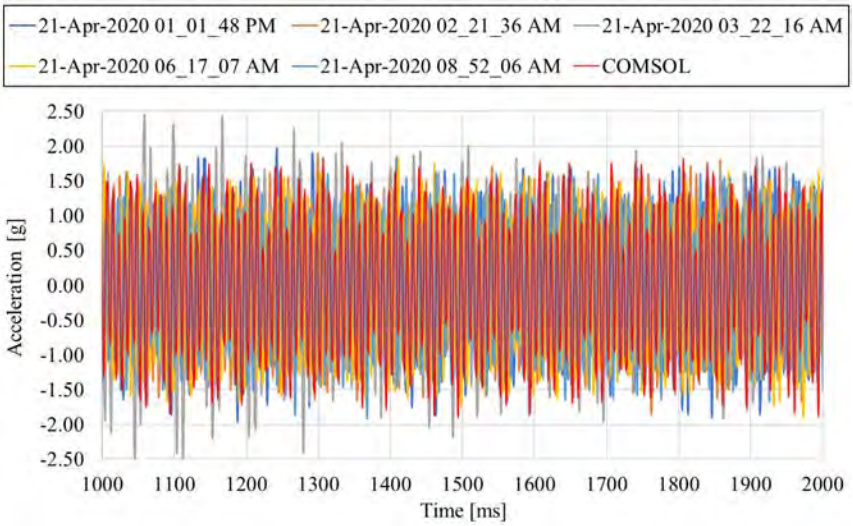

Figure 22. Vertical (axial) acceleration for the MOB location collected at five different time instances and the simulated vibration waveform.

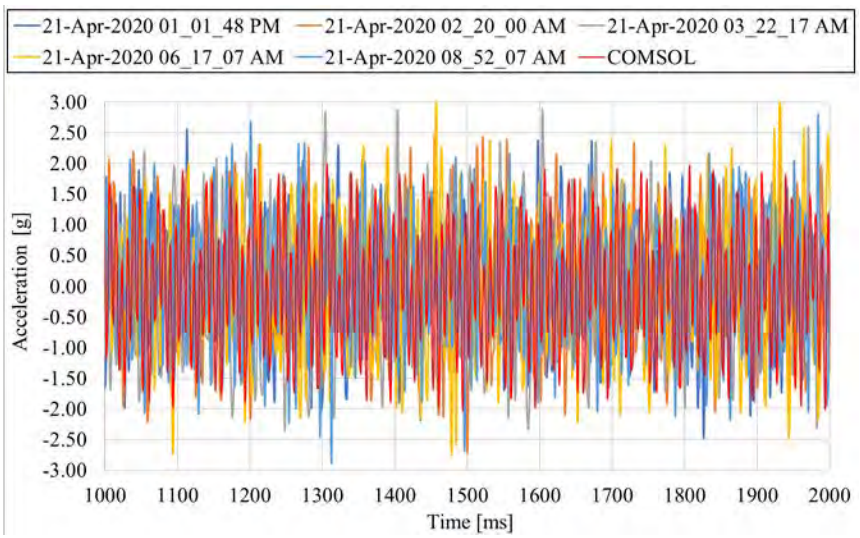

Figure 23. Radial acceleration for the MOB location collected at five different time instances and the simulated vibration waveform.

For a quantitative comparison with the actual vibration waveform, these numerically obtained vibration signals are transformed into PSD plots and presented in Figure 24–Figure 27. As noticed from these PSD plots, three dominant frequencies were returned using the current numerical model (i.e., at 30 Hz, 100 Hz, and 120 Hz).

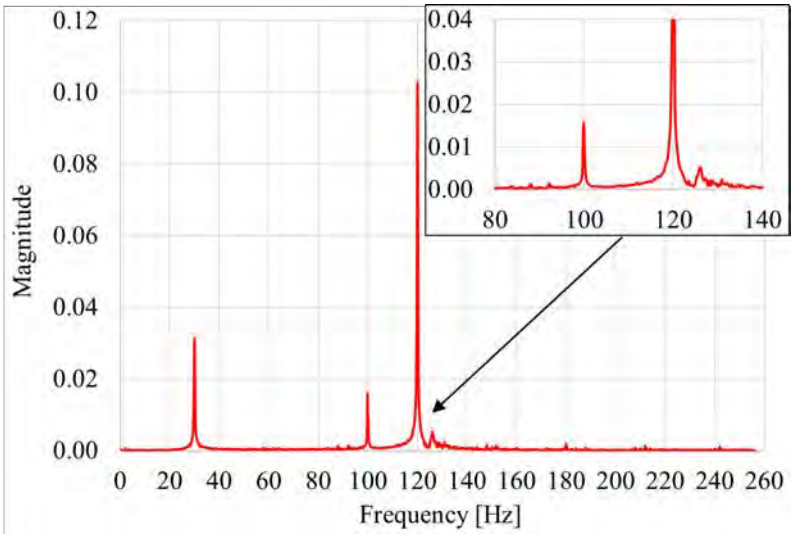

Figure 24. PSD plot for vertical (axial) simulated vibration waveform for the MIB location.

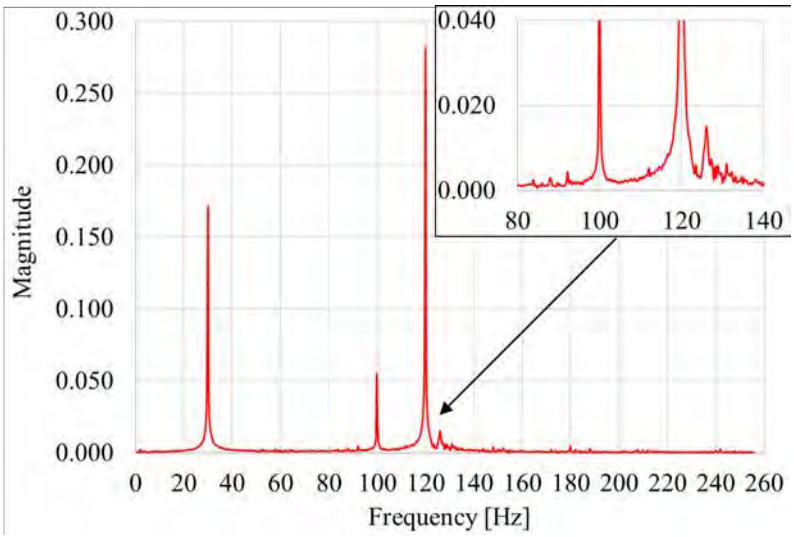

Figure 25. PSD plot for radial simulated vibration waveform for the MIB location.

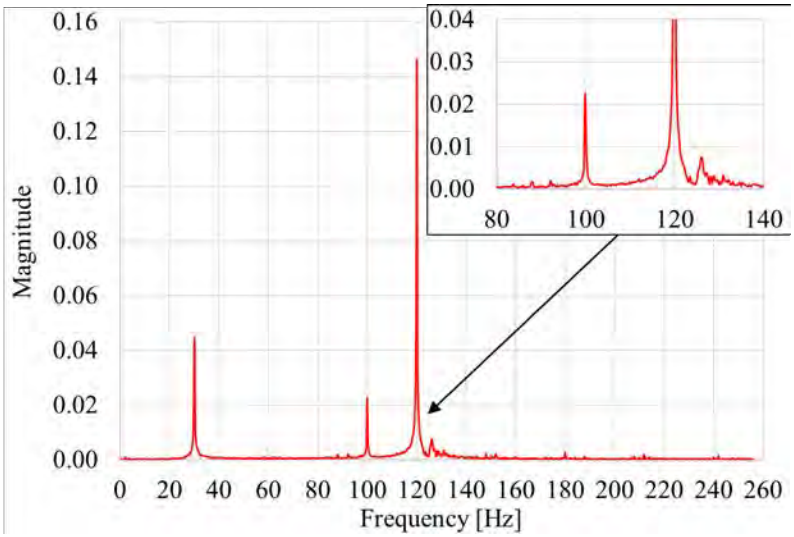

Figure 26. PSD plot for vertical (axial) simulated vibration waveform for the MOB location.

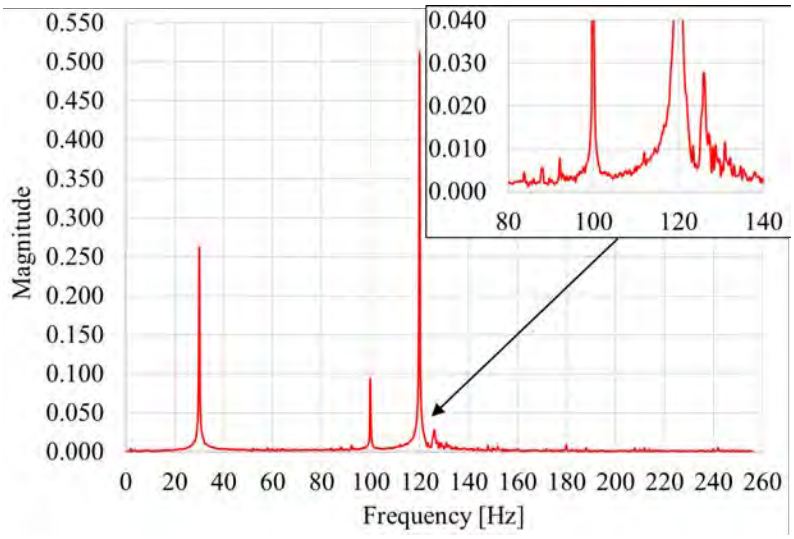

Figure 27. PSD plot for radial simulated vibration waveform for the MOB location.

5. DISCUSSION

As noted in the PSD plots (Figure 11–Figure 14) for actual vibration waveform, three dominant frequency are obvious (i.e., at 30 Hz, 100 Hz, and 120 Hz). Moreover, these plots show that the experimental data is consistent with no instances of deviations between each measurement. In addition to dominant frequency, one can also notice other frequencies of smaller amplitude, especially for radial acceleration for the MOB location (Figure 14). Direct comparison of these PSD plots with the numerically obtained vibration waveform for both directions and at both measuring locations (Figure 24–Figure 27) reveals that experimental data signals have additional information and are more noisy than the computational results. This is expected because interactions below the mounting surface and other aspects of operation of these CWP motors were ignored or simplified as part of modeling assumptions.

The relatively sharp peaks at 30 Hz, 100 Hz, and 120 Hz in Figure 24–Figure 27 prove that the observed (expected) behaviors in the actual vibration waveform were successfully captured by the present numerical model even though small peaks at other frequencies were not. To compare these two approaches more closely, root mean square error (RMSE) is computed (see Table 3) between the PSD plots obtained using the actual and simulated vibration waveforms at both the locations and in both directions (Figure 11–Figure 14). Figure 28–Figure 31 show the square of the difference between the PSD plots obtained using the actual and simulated vibration waveforms.

Table 3. RMSE for each experimental dataset compared with the numerical results.

MIB: axial direction		**MIB: radial direction**	
Data (time instance)	**RMSE**	**Data (time instance)**	**RMSE**
D1: 21-Apr-2020 01_20_00 PM	0.0027	D6: 21-Apr-2020 01_20_00 PM	0.0132
D2: 21-Apr-2020 02_20_00 AM	0.0019	D7: 21-Apr-2020 02_21_22 AM	0.0130
D3: 21-Apr-2020 03_20_00 AM	0.0018	D8: 21-Apr-2020 03_22_02 AM	0.0131
D4: 21-Apr-2020 06_20_00 AM	0.0019	D9: 21-Apr-2020 06_21_51 AM	0.0131
D5: 21-Apr-2020 09_00_00 AM	0.0020	D10: 21-Apr-2020 08_56_51 AM	0.0132
MOB: axial direction		**MOB: radial direction**	
Data (time instance)	**RMSE**	**Data (time instance)**	**RMSE**
D11: 21-Apr-2020 01_01_48 PM	0.0050	D16: 21-Apr-2020 01_01_48 PM	0.0230
D12: 21-Apr-2020 02_21_36 AM	0.0042	D17: 21-Apr-2020 02_20_00 AM	0.0230
D13: 21-Apr-2020 03_22_16 AM	0.0042	D18: 21-Apr-2020 03_22_17 AM	0.0230

D14: 21-Apr-2020 06_17_07 AM	0.0042	D19: 21-Apr-2020 06_17_07 AM	0.0231
D15: 21-Apr-2020 08_52_06 AM	0.0042	D20: 21-Apr-2020 08_52_07 AM	0.0231

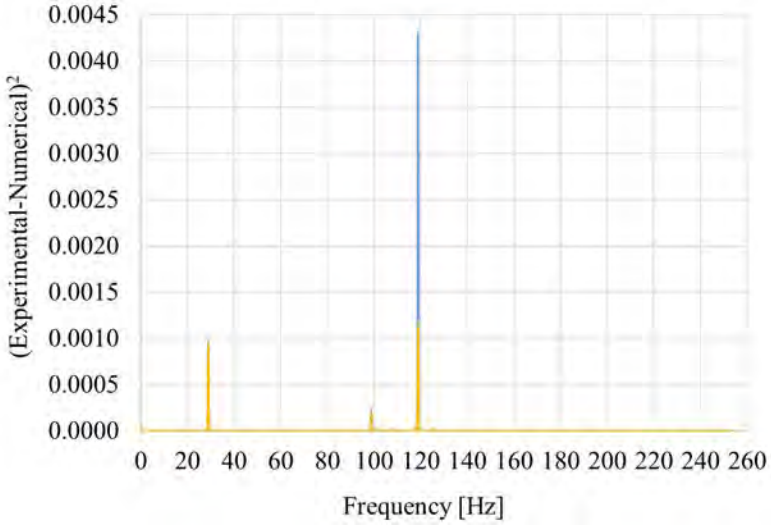

Figure 28. Squared difference between the actual and numerical PSD plots for axial acceleration for the MIB location collected at different time instances.

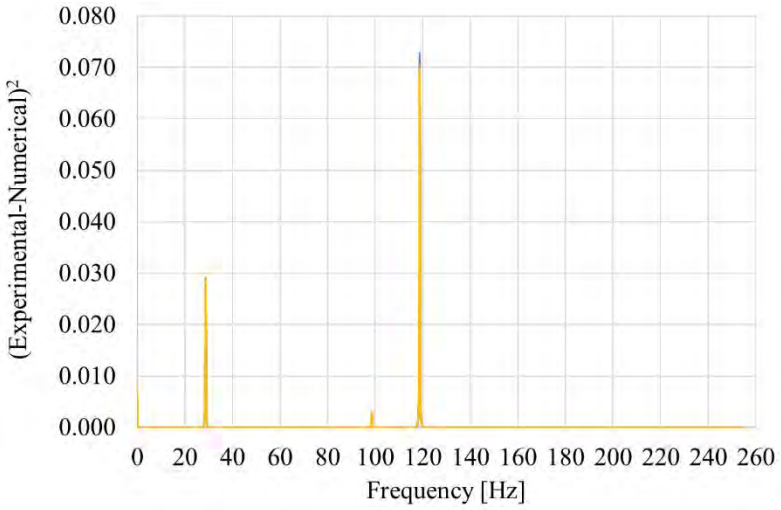

Figure 29. Squared difference between the actual and numerical PSD plots for radial acceleration for the MIB location collected at different time instances.

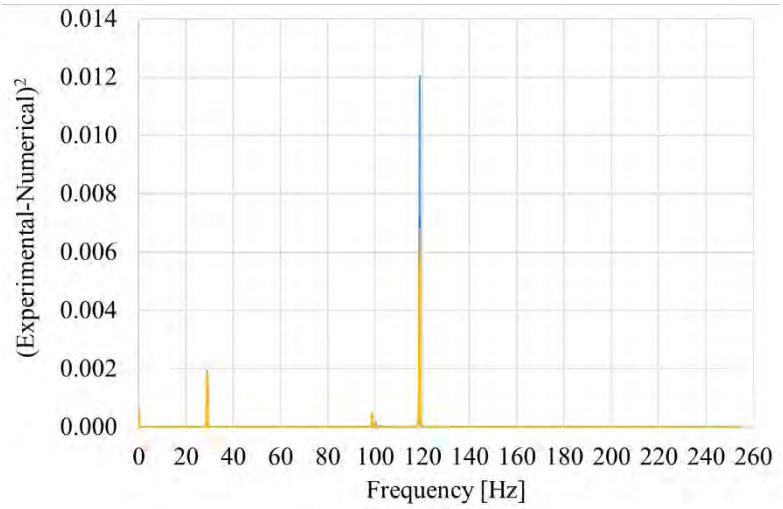

Figure 30. Squared difference between the actual and numerical PSD plots for axial acceleration for the MOB location collected at different time instances.

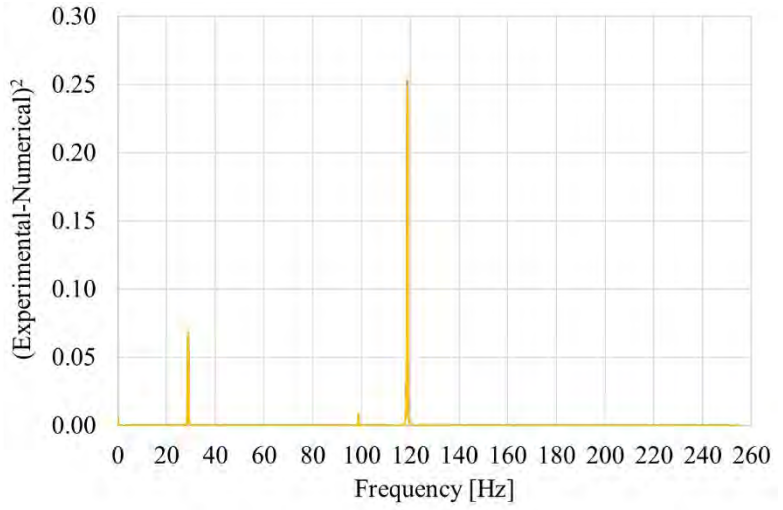

Figure 31. Squared difference between the actual and numerical PSD plots for radial acceleration for the MOB location collected at different time instances.

6. HYBRID MODELING RESULTS

In this section, a linear machine learning approach was trained and validated as part of the hybrid modeling. The RMSE values (Table 3) along with computational model inputs such as Young's modulus, mechanical forces, and thickness of casing and motor stand are used to train a ridge regression model. In ridge regression, the solution is obtained by minimizing the combination of both the sum of squared errors and the norm of the weight vector, denoted as W. Mathematically, is expressed as,

$$\underset{W}{argmin}\ \lambda\|W\|_2^2 + \|Y - XW\|_2^2 \tag{1}$$

where λ is the regularization parameter that determines the trade-off between the error and the smoothness of the solution; Y is the response vector; X is the input matrix; and W is the model coefficient vector, i.e., weights. The value of λ is computed using the k-fold cross validation method. The analytical solution of Equation (1) provides the ridge regression coefficients,

$$W_{ridge} = (X^T X + \lambda I)^{-1} X^T Y \quad (2)$$

where I is the identity matrix.

As mentioned earlier, five vibration measurements at four locations were collected at different time instances, resulting in twenty (20) data sets that can be used to develop and test the hybrid model. Single vibration data sets from each of the four locations were randomly selected to develop a hybrid model. The developed hybrid model is tested on the remaining sixteen (16) vibration data sets. Numerical model outputs from the same testing vibration data were used to evaluate the performance of the hybrid model.

The results of initial hybrid model and numerical model are summarized in Table 4. For the results presented in Table 4, the third measurement across all four locations was used to train the hybrid model.

Table 4. RMSE for estimated PSD using hybrid and numerical models on sixteen (16) testing data.

MIB: axial direction			**MIB: radial direction**		
Data Label	**RMSE**		**Data Label**	**RMSE**	
	Numerical Model	**Hybrid Model**		**Numerical Model**	**Hybrid Model**
D1	0.0027	0.0020	D6	0.0132	0.0110
D2	0.0019	0.0011	D7	0.0130	0.0105
D4	0.0019	0.0010	D9	0.0131	0.0109
D5	0.0020	0.0014	D10	0.0132	0.0109
MOB: axial direction			**MOB: radial direction**		
Data (time instance)	**RMSE**		**Data (time instance)**	**RMSE**	
	Numerical Model	**Hybrid Model**		**Numerical Model**	**Hybrid Model**
D11	0.0050	0.0010	D16	0.0230	0.0195
D12	0.0042	0.0009	D17	0.0230	0.0191
D14	0.0042	0.0012	D19	0.0231	0.0194
D15	0.0042	0.0011	D20	0.0231	0.0191

7. SUMMARY AND PATH FORWARD

The work presented in this report describes the technical basis to develop a digital twin of the circulating water pump motor, using a hybrid modeling approach in order to capture both the deterministic and stochastic operation characteristics. A detailed first principle model of the circulating water pump motor is developed using the multipurpose finite element software COMSOL Multiphysics. Geometry and material properties were obtained from circulating water system manual. The actual vibration measurement used to compare the simulated vibration response and to train the data-driven approach were obtained from installed wireless vibration sensors. The outcomes of the report lay the foundation to develop a comprehensive digital twin of the circulating water system by taking into consideration different operating dynamics.

The next year of this research project includes the following R&D tasks, performed in collaboration with PSEG Nuclear, LLC:

- Evaluating the hybrid model performance using additional vibration waveforms collected under different operating conditions
- Enhancing the hybrid model by evaluating the relaxation of some assumptions
- Utilizing the hybrid model of the CWS to develop predictive fault signatures enabling development of robust diagnosis and prognosis of health of the circulating water system and decision-making capability as part of the PdM strategy.

8. REFERENCES

1. McJunkin, T., V. Agarwal, N. J. Lybeck, and C. Rasmussen 2015. “Online Monitoring of Induction Motors,” INL/EXT-15-36681, Idaho National Laboratory.
2. Agarwal, V., N. J. Lybeck, and B. T. Pham. 2014. “Diagnostic and Prognostic Models for Generator Step-up Transformers,” INL/EXT-14-33124, Idaho National Laboratory.
3. Agarwal, V., N. J. Lybeck, L. C. Matacia, and B. T. Pham. 2013. “Demonstration of Online Monitoring for Generator Step-up Transformers and Emergency Diesel Generators,” INL/EXT-13-30155, Idaho National Laboratory.
4. Goss, N., et al. 2020. “Integrated Risk-Informed Condition Based Maintenance Capability and Automated Platform: Technical Report 1,” PKM-DOC-20-0013, PKMJ Technical Services.
5. Agarwal, V., et al. 2019. “Deployable Predictive Maintenance Strategy Based on Models Developed to Monitor Circulating Water System at the Salem Nuclear Power Plant,” INL/LTD-19-55637, Idaho National Laboratory.
6. Idaho National Laboratory. 2019. “Light Water Reactor Sustainability Program, Integrated Program Plan,” INL/EXT-11-23452, Rev. 8, Idaho National Laboratory.
7. Hines, J.W., Miller, D.W., and Hajek, B. K. “Fault detection and isolation: A Hybrid Approach,” *Topical Meeting of Nuclear Plant Instrumentation & Control and Human-Machine Interface Technologies*, 1995.
8. Hines, J. W., D. W. Miller, and B. K. Hajek. A Hybrid Approach for Detecting and Isolating Faults in Nuclear Power Plant Interacting Systems. *Nuclear Technology*, vol. 115, no. 3, 1996.
9. Gribok, A. V., Buller, M. J., and Reifman, J. “Individualized short-term core temperature prediction in humans using biomathematical models,” *IEEE Transactions on Biomedical Engineering*, vol. 55, no. 5, pp. 1477-1487, 2008.
10. K. Technologies, "KCF Vibration Sensor Node SD-VSN-3," [Online]. Available: https://www.kcftech.com/smartdiagnostics/products/sensors.html. [Accessed May 2020].
11. "KCF Wireless Interference and SmartDiagnostics®," [Online]. Available: https://www.kcftech.com/smartdiagnostics/resources/whitepapers/Application%20Note%20-%20Wireless%20Interference%20and%20SmartDiagnostics.pdf. [Accessed May 2020].
12. Goss, N., et al. 2020. “Integrated Risk-Informed Condition Based Maintenance Capability and Automated Platform: Technical Report 1,” PKM-DOC-20-0013, PKMJ Technical Services.